applied sciences

MDPI

Article

Full-Frequency Vibroacoustic Modeling of a Ballistic Re-Entry Aeroshell and Validation through Diffuse Field Acoustic Testing

Maxence Claeys *, Hélène Valle Canas and Benoit Alcoverro

CEA/CESTA, 15 Avenue des Sablières, CS60001, 33114 Le Barp, France; helene.vallecanas@protonmail.com (H.V.C.); benoit.alcoverro@cea.fr (B.A.)
* Correspondence: maxence.claeys@cea.fr

Featured Application: Simulation of in-flight vibrations of aeronautical structures.

Abstract: During ballistic flight, a re-entry vehicle is subjected to high-level structural vibrations due to pressure fluctuations on its bounding surface. The aim of this work is to simulate this structural vibration response. The first step, which is not covered in this study, is the modeling of pressure fluctuations using aerodynamic simulation results. The second step is the simulation of the vibroacoustic response. In this study, the full-frequency vibroacoustic modeling of a metal shell representing a re-entry vehicle aeroshell is developed. The low-frequency response is computed using a FEM–BEM model while Statistical Energy Analysis is used for high-frequency behavior. The validation of these models is based on a ground experiment with controlled diffuse-field acoustic loading. A dedicated reverberation chamber was developed with loudspeaker excitation. The simulation results are compared with the experimental results. In the low-frequency range, simulation helps to understand the measured response spectra by highlighting the acoustic resonances and scattering phenomena. In the high-frequency range, an experimental identification of the damping loss factors and SEA modeling of each subsystem using an FE–SEA approach provides a predictive simulation of the vibration-response spectrum. In this application, FEM–BEM and SEA models are complementary in simulating full-frequency vibroacoustic responses.

Keywords: vibroacoustic simulation; diffuse acoustic field testing; FEM; BEM; SEA

Citation: Claeys, M.; Valle Canas, H.; Alcoverro, B. Full-Frequency Vibroacoustic Modeling of a Ballistic Re-Entry Aeroshell and Validation through Diffuse Field Acoustic Testing. *Appl. Sci.* **2022**, *12*, 5397. https://doi.org/10.3390/app12115397

Academic Editors: Roberto Citarella, Luigi Federico and Venanzio Giannella

Received: 22 March 2022
Accepted: 11 May 2022
Published: 26 May 2022

1. Introduction

The simulation of in-flight structural vibrations of an aeronautical vehicle requires modeling pressure fluctuations on its bounding surface and modeling the vehicle. The first diagram in Figure 1 represents the target simulation process. In-flight experiments are rare, and the ability of the simulation process to reproduce the measured dynamic behavior depends on:

- the Computational Fluid Dynamics (CFD) simulation of the flow around the vehicle,
- the pressure fluctuation dimensionless model, and
- the vehicle vibroacoustic model.

These three steps must be validated separately. The CFD simulation and the Turbulent Boundary Layer (TBL) pressure-fluctuation models are usually validated using wind tunnel experiments. The development of pressure-fluctuation models started in the 1960s with, in particular, works by Corcos [1] and Bull [2]. Many improvements have been proposed since then.

For subsonic flows without a pressure gradient, Goody's model has proven to be one of the most relevant models to date, fitting with several wind tunnel experiments [3]. Dedicated experiments have also focused on high Mach numbers for the modeling of ballistic vehicles. Houbolt [4] and Lowson [5] proposed the first models in the 1960s; Laganelli and Howe [6] proposed improvements in the 1980s; and, more recently, these models have been challenged by new experiments (see [7,8] for example).

These models have all been validated using wind tunnel experiments, which is the second process shown in Figure 1. The alternate validation process is the direct measurement of in-flight pressure fluctuations. Such data during hypersonic flight have been measured during the HI-FIRE experiment [9]. However, this type of measurement is extremely rare.

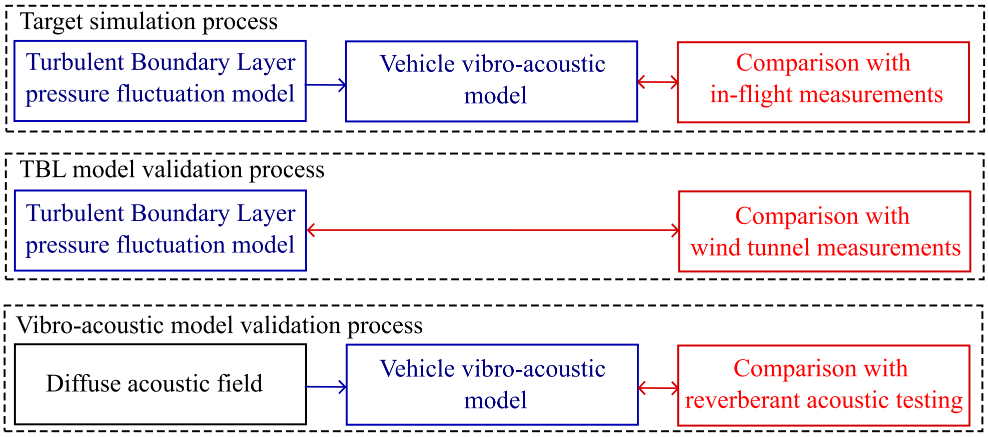

Figure 1. Simulation and validation processes. The blue rectangles represent steps where various models can be chosen. The "Diffuse Acoustic Field" rectangle is colored black because it corresponds to a unique analytical definition. The red rectangles represent comparison with the experiment steps.

Once the pressure-fluctuation model was chosen and the turbulent boundary layer simulated using dedicated CFD simulation, the surface dynamic load was defined in terms of the Power Spectral Density (PSD) level and surface correlation laws as a function of frequency. The response of a vibroacoustic model to this input can be computed. The full-frequency modeling of the vehicle must then be performed.

In the low-frequency range, the most widely used modeling methods are based on the Finite Element Method (FEM). Once the vehicle has been modeled using structural finite elements, applying a distributed random dynamic pressure—which is correlated in space and frequency—is not trivial. A few articles have tackled this issue. Among them, Hong and Shin proposed an equivalent uncorrelated random pressure field [10], and Bonness et al. investigated several approaches to perform the computation efficiently [11].

The most widely used method for applying an acoustic loading to a structural finite element model is the modeling of the air volume surrounding the structure using the Boundary Element Method (BEM). Many examples may be found for automotive or aeronautical applications (see for example [12–14]). The combination with turbulent boundary layer pressure fluctuation loading has been studied, in particular, by Mongomery for an aeronautical application [15] and by Li et al. with several correlation models applied on a plate [16].

At higher frequencies, the relevance of a finite element model decreases as the size of the elements cannot be considered small in comparison to the wavelengths of the vibration modes. Statistical Energy Analysis (SEA) [17] enables the prediction of high-frequency averaged vibration responses with a low computational cost. The response of an SEA model to turbulent boundary layer noise is often computed for the prediction of internal aircraft noise. For example, a recent SEA modeling of an aircraft fuselage was developed in [18].

Combining a Finite Element model and a SEA model may result in a full-frequency model of the structure. However, between high and low-frequency ranges, there may be a range where neither finite elements nor SEA are relevant. Many "mid-frequency" methods have been proposed to bridge this gap. Most of them are described in the workbook [19]. Various full-frequency modeling methods may be chosen.

Certain wave-based methods, such as the variational theory of complex rays [20] proposed a unique full-frequency framework. Industrial studies often prefer a combination of a FE model with a SEA model and may use a hybrid FE–SEA model [21] for mid-frequencies.

An example of such full-frequency modeling of an aircraft fuselage is described in [22]. In this article, a FEM–BEM model and a SEA model of a ballistic re-entry aeroshell are developed. The final aim of such modeling is the computation of in-flight vibrations, which is the first process shown in Figure 1. The simulation results depend both on the modeling of the structure and the modeling of the in-flight pressure fluctuations. In this article, a process for validating the structure model alone is deployed—the third process shown in Figure 1.

The ground experiment chosen is diffuse acoustic testing. As well as turbulent boundary layer noise, diffuse acoustic noise is a dynamic pressure load correlated in space and frequency. Using a dedicated test facility, this load can be precisely controlled. Such experiments are widely used for the modeling of plates and panels [23,24]. Fewer test–simulation comparisons have been published on industrial structures (see [25] for example).

The vibroacoustic response of a hypersonic aircraft external shape to a diffuse acoustic field has recently been studied by Pr. Yunjun Yan's team. A FEM–BEM model [26], a SEA model [27] and a hybrid FE–SEA model [28] of the structure have been developed. Simulations have been compared with diffuse acoustic testing experiments.

The approach deployed here uses diffuse field experimentation as a validation tool. The study focuses on the understanding, modeling and simulation of vibroacoustic phenomena. The aim is to simulate and interpret resonances in the low-frequency range on the one hand, and to simulate average responses at higher frequencies on the other. The experimental setup (test structure, diffuse acoustic testing facility and measurement tools) is described in the first section of this article. The second and third sections describe the model and the results obtained by FEM–BEM and SEA, respectively. Finally, the results obtained with the two models are combined to perform a full-frequency test–simulation comparison.

2. Experiments

2.1. The HB–2 Test Structure

The HB–2 test structure is shown in Figure 2. It is composed of an envelope and a bottom both made of an aluminum alloy. It represents the aeroshell of a ballistic vehicle without a heat shield. The external profile, designated "HB–2" was defined in the scientific literature for aerodynamic study purposes [29]. The diameter of the cylinder was set at 200 mm, resulting in a total height of the envelope of 980 mm. The bottom contains six circular holes, which provide a direct link between the internal and external air volumes. The internal profile of the envelope includes stiffeners and flanges. The structure is suspended in the air to obtain the free boundary conditions.

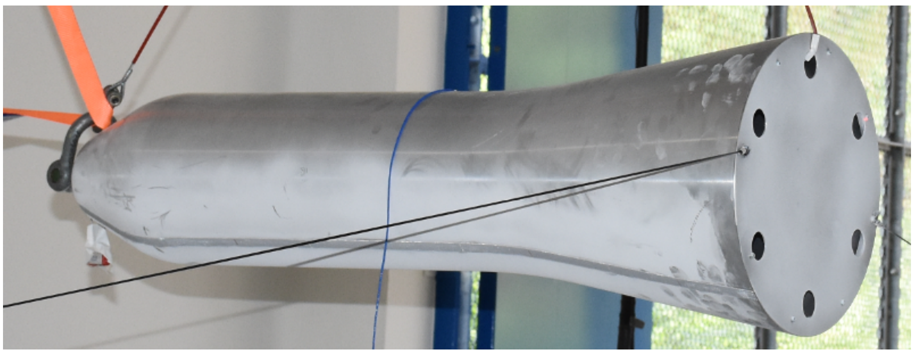

Figure 2. HB–2 structure suspended in the air.

2.2. Diffuse Acoustic Field Experiments

A reverberation chamber was developed at the CEA/CESTA site. This chamber is a rectangular shaped room (7.5 m $\times$ 4.5 m $\times$ 6 m) with painted concrete walls that ensures octave band RT60 upper of 2 s from 250 Hz to 15 kHz. The diffuse field is obtained from 250 Hz (Schroeder frequency). The excitation is provided by two identical assemblies of loudspeakers, and one of them is visible in Figure 3.

Each assembly includes 12 mid-frequency loudspeakers (100–2000 Hz) and five high-frequency loudspeakers (1000–15,000 Hz). The position of the mid-frequency loudspeakers, a dedicated waveguide for the high-frequency loudspeakers and the natural reverberation properties of the chamber ensure a homogeneous diffuse acoustic field in the room at any point situated more than two meters away from the excitation assemblies. At frequencies below 250 Hz, the modal response is dominant.

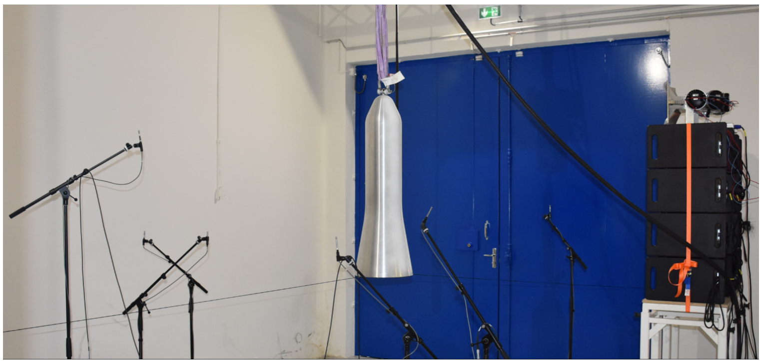

Figure 3. HB–2 structure in the vertical configuration in the reverberation chamber with the six control microphones and the loudspeakers on the right.

This acoustic pressure field is measured by six microphones placed evenly and randomly around the structure. The mean of these six measurements serves as the control channel, in such a way that the acoustic pressure power spectral density (PSD) can be controlled precisely. The excitation chosen is a pink noise between 100 Hz and 15 kHz:

$$S_p(\omega) = S_p(100\text{ Hz})\left(\frac{2\pi\,100\text{ Hz}}{\omega}\right) \tag{1}$$

$S_p(100\text{ Hz})$ is calculated to control the overall acoustic pressure root mean square (RMS) level. Figure 4 shows this control and the resulting mean acoustic pressure PSD for a 110 dB SPL level.

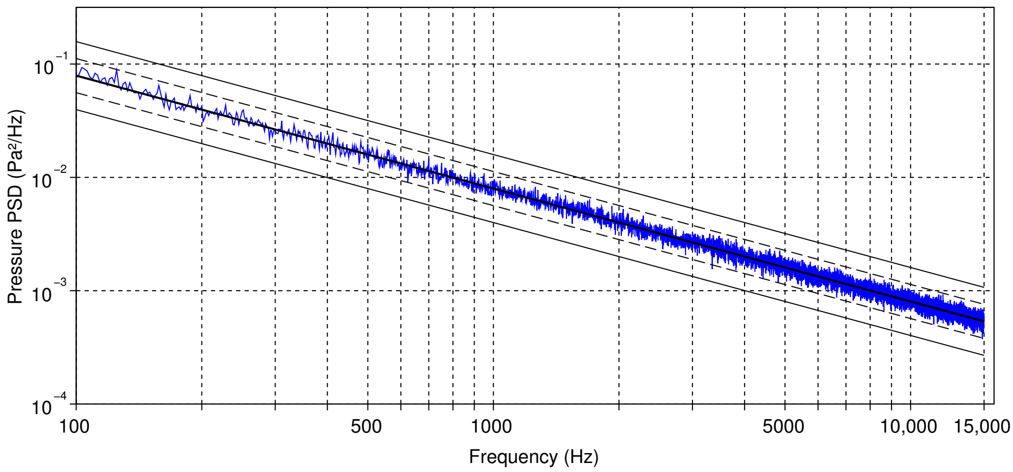

Figure 4. The mean pressure PSD of the six microphones (blue) compared with the control (thick line), ±3 dB envelope (dashed lines) and ±6 dB envelope (thin lines).

2.3. Scanning Laser Vibrometer Measurements

The structural response is measured using a scanning laser vibrometer situated in an adjacent room and protected by a glass window (see Figure 5). Scanning laser vibrometry enables non-intrusive measurements (no mass added to the surface) and a large number of measurement points. This large amount of experimental data proves to be useful for the validation of the SEA model—the responses of which are averaged in space. However, measurements can only be performed on the external surfaces that are visible from the adjacent room through the protective window. Two configurations of the structure were set up.

In the vertical configuration, shown in Figure 3, the response of the external envelope was measured, while the response of the bottom was measured in the horizontal configuration, shown in Figure 5. Preliminary tests have shown that the presence of the test structure, regardless of its orientation, in the middle of the chamber, has a negligible effect on the acoustic sound field. Furthermore, with scanning laser vibrometry, the measurements at different points are not synchronous but sequential. The Power Spectral Density of each measurement point is computed; however, the cross power spectral densities cannot be computed.

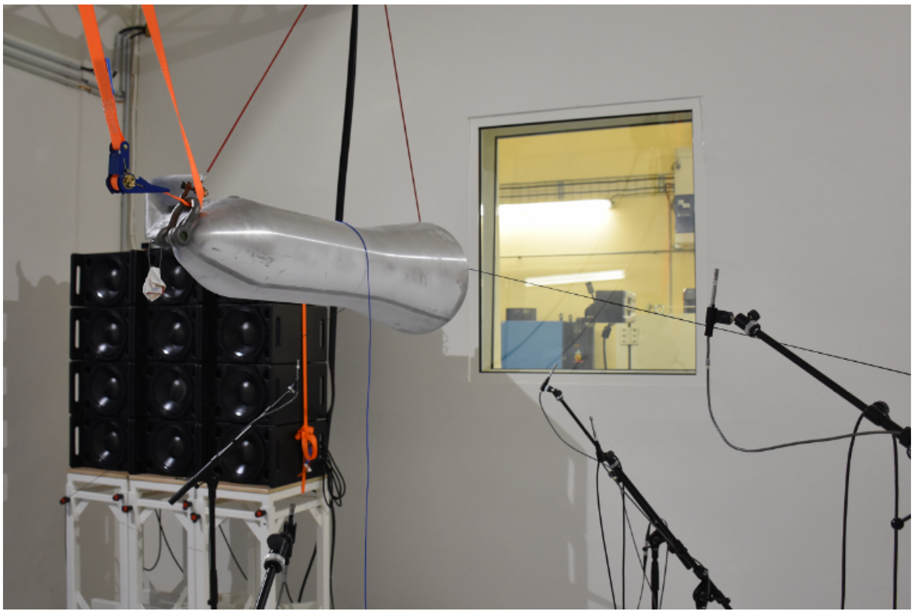

Figure 5. The HB–2 structure in the horizontal configuration in the reverberation chamber and, behind the window, the scanning laser vibrometer.

3. Finite Element Models

3.1. Structural Finite Element Model

A Finite Element Model of the HB–2 structure was built using Abaqus, as shown in Figure 6. The maximum element length on the envelope was 5 mm. The two parts (bottom and envelope) were tied together. The first modes, in the (5 Hz–2500 Hz) frequency range, were computed. The dynamics equation was projected onto this modal basis of size $N_m = 93$. The modal frequency transfer functions are defined by:

$$H_k(\omega) = \left(m_k \left({\omega_k}^2 - 2j\xi_k \omega_k \omega + \omega^2 \right) \right)^{-1} \tag{2}$$

where, for every mode k, ω_k is the proper angular frequency, m_k is the modal mass, and ξ_k is the modal damping coefficient. This modal damping coefficient was set as 0.3% for all modes. This constant value was chosen to fit the first experimental data obtained in the reverberant chamber. An additional experiment dedicated to the identification of the Coupling Loss Factors of the SEA method (see Section 4.2) confirmed this modeling hypothesis: the average modal damping of the first structural modes wa 0.3%. The proper vector is denoted $\Phi_{\mathbf{k}}$.

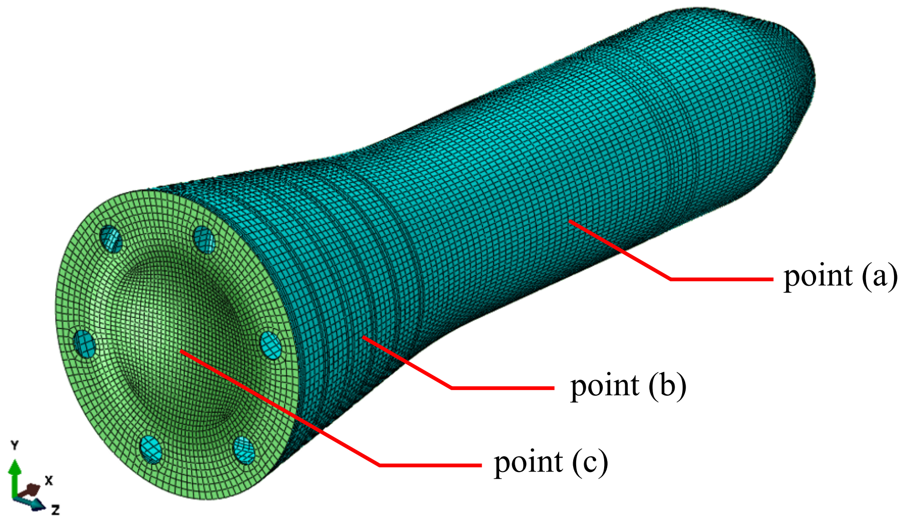

Figure 6. HB–2 Finite Element Model and location of the three points studied.

When the air volume surrounding the structure is not modeled, no scattering effect is considered. The dynamic pressure loading on the external surface of the structure is defined by the controlled mean PSD in the reverberant chamber as shown in Equation (1). The cross power spectral density is known analytically for a diffuse field in an open air volume:

$$S_p(\mathbf{x_1}, \mathbf{x_2}, \omega) = S_p(\omega).\mathrm{sinc}\left(\frac{\omega\|\mathbf{x_1} - \mathbf{x_2}\|}{c}\right) \tag{3}$$

where c is the speed of sound.

The computation of the dynamic response of the structure to that dynamic load can be directly performed. This requires the computation of the cross spectral modal forces (or joint modal acceptances) that are defined by:

$$F_{k_1k_2}(\omega) = \sum_{\mathbf{x_1}\in\mathcal{S}} \sum_{\mathbf{x_2}\in\mathcal{S}} S_p(\mathbf{x_1}, \mathbf{x_2}, \omega)\left(\Phi_{k_1}(\mathbf{x_1})^* \,\mathbf{dx_1}\right)\left(\Phi_{k_2}(\mathbf{x_2})^* \,\mathbf{dx_2}\right) \tag{4}$$

$\left(\Phi_{k_1}(\mathbf{x_1})^* \,\mathbf{dx_1}\right)$ is the projection of the 3D vector $\Phi_{k_1}(\mathbf{x_1})$ on the locally oriented surface in point $\mathbf{x_1}$. Each evaluation of $F_{k_1k_2}(\omega)$ requires a double integration over the external surface $\mathcal{S}$, which is computationally expensive.

The computation method used in this study is implemented in the vibroacoustics simulation software Wave6. The computation of the cross-spectral modal forces is equivalent to the computation of the acoustic dynamic stiffness matrix [30]. Instead of computing this matrix directly in the modal basis, an intermediate basis is used. This basis is a wavelet discretization of the surface. The method is detailed in [31]. Once the acoustic dynamic stiffness matrix has been evaluated on this wavelet basis, it can be easily projected onto any mode shape, at any frequency, which enhances the computational efficiency of the method.

This first method was used to compute the vibroacoustic response of the HB–2 structure without any acoustic phenomena (scattering or internal acoustic resonances). The vibroacoustic model of the system is then improved by modeling the surrounding air volumes using a Boundary Element Model. A second model was implemented in which only the external air volume is modeled, and thereby the scattering effects are simulated. A third model is then implemented in which both the external and internal air volumes are modeled, so that the scattering effects and internal acoustic resonance phenomena are simulated simultaneously. The second and third models are described in the next section, and the results obtained with the three models are compared together.

3.2. Boundary Element Models

In order to model the surrounding air volume, a closed external surface of the structure is defined and meshed as illustrated in Figure 7, left. The external volume of this surface is defined as a Boundary Element Method (BEM) subsystem. A volume diffuse acoustic field excitation is defined in this subsystem. This excitation is implemented using the reciprocity relationship between direct field radiation and diffuse reverberant loading [30]. This BEM subsystem is then coupled to the FEM subsystem through a surface junction. The boundary condition of the BEM subsystem becomes a structural coupling, and the pressure loading on the FEM subsystem is equal to the acoustic pressure at the BEM boundary. This strong coupling creates a classical FEM–BEM model [14]. The boundary element method in Wave6 is based on a mixed direct/indirect variational formulation and uses acceleration methods for large problems along with a direct rather than iterative linear solver (in order to avoid the convergence issues often encountered with iterative solvers and boundary integral equations).

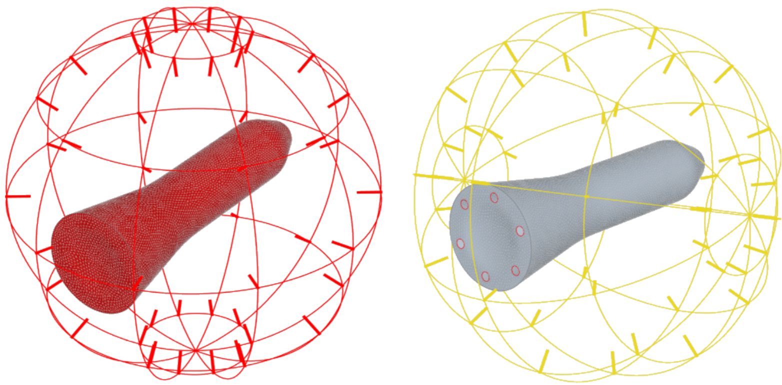

Figure 7. HB–2 Boundary Element Models in Wave6: left, model of the external air volume; and right, model of external and internal air volumes.

Another BEM subsystem is defined to model both the external and internal air volumes. The external surface of the structure is defined and meshed excluding the six circular surfaces corresponding to the holes in the bottom of the structure (see Figure 7, right). This open surface makes it possible to create a BEM subsystem that includes the internal and external air volumes of the structure.

In this subsystem, the meshed surface is "double-sided wetted" with a discontinuity in the acoustic pressure field from one side of the surface to the other. The coupling with the FEM subsystem is then performed as a surface junction. This coupling associates the external faces of the FEM subsystem with the external side of the BEM surface and, reciprocally, the internal faces of the FEM subsystem with the internal surface of the BEM subsystem.

3.3. FEM–BEM Simulation Results

The simulation results obtained at the center of the bottom with the three models are compared in Figures 8 and 9. In Figure 8, the results at the center of the envelope (point (a)) are plotted. The differences between the blue and the green curves indicate the influence of scattering on the structural response. The spectra obtained are similar (the same resonances); however, the response levels are different. Scattering phenomena change the cross spectra modal forces. On these results on the envelope, there is little difference between the FEM–BEM models for when the internal air volume is modeled (red curve) versus not (blue curve).

However, in Figure 9, great differences are observed between the two FEM–BEM models at the center of the bottom. When the internal air volume is modeled (red curves), many additional resonance peaks are observed. These correspond to acoustic resonance phenomena. These acoustic resonances generate new peaks away from the main structural resonances but may also significantly affect the response level in the vicinity of these main structural modes. Figure 9 illustrates this influence near the first bottom mode (408 Hz).

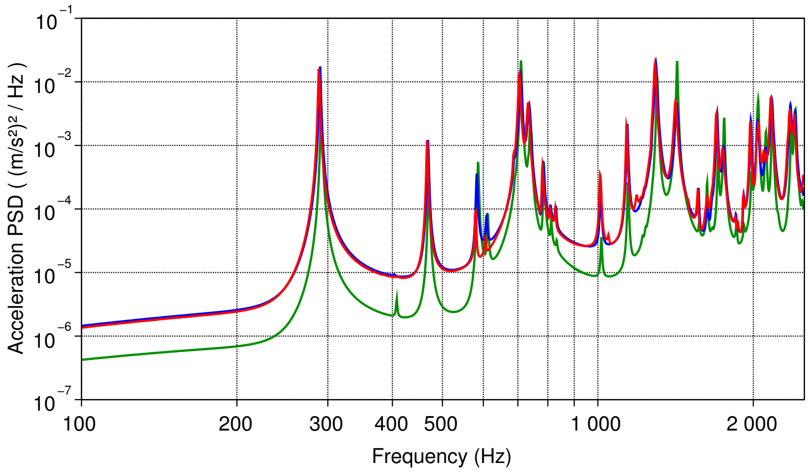

Figure 8. HB–2 structural response (acceleration PSD) at the center of the envelope, point (a) in Figure 6, simulated using the FEM model alone (green), the BEM subsystem of the external air volume (blue) and the BEM subsystem of both internal and external air volumes (red).

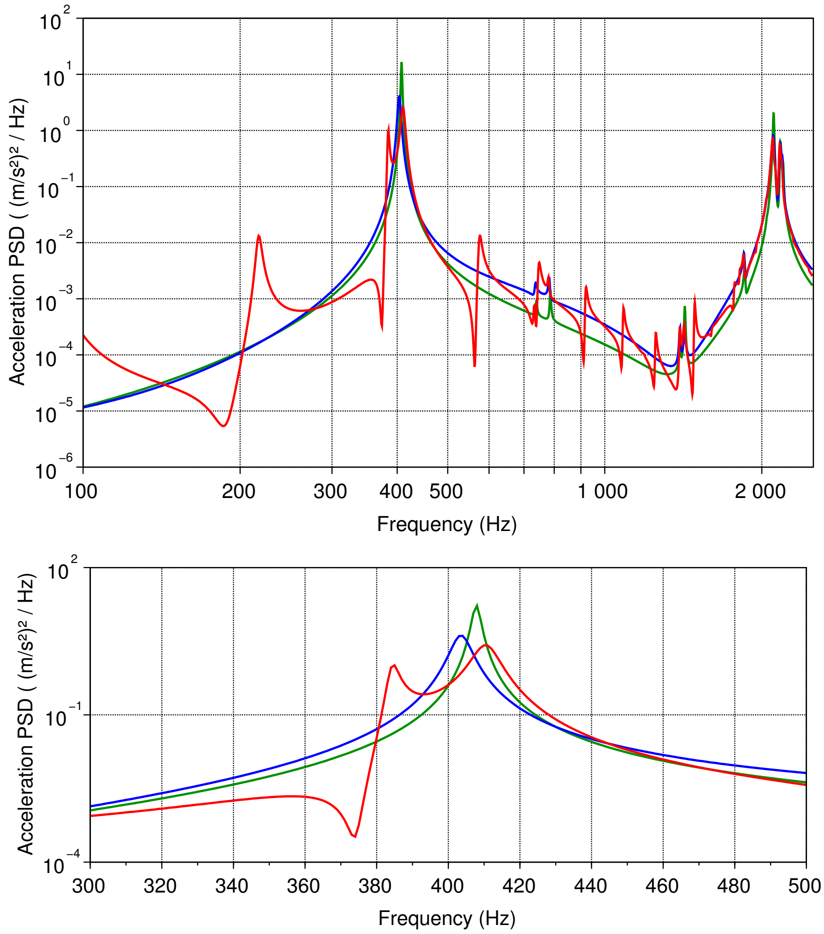

Figure 9. HB–2 structural response (acceleration PSD) at the center of the bottom, point (c) in Figure 6, simulated using the FEM model alone (green), the BEM subsystem of the external air volume (blue) and the BEM subsystem of both internal and external air volumes (red). A zoom in the vicinity of the first structural bottom mode (408 Hz) is added.

Modeling the air volumes surrounding the structure thus implies clear effects on the structural responses; yet, the main resonances and the RMS levels remain similar. The RMS levels corresponding to the three simulations of Figure 9 are 10.86 m·s^{-2} (FEM model, green curve), 9.43 m·s^{-2} (FEM–BEM model with external air volume modeled, blue curve) and 9.07 m·s^{-2} (FEM–BEM model with external and internal air volumes modeled, red curve).

The differences between the simulation results obtained with the three models aids in understanding the effects of each vibroacoustic phenomenon in the structure response. The modeling method chosen for the comparison with experiments is the most complete: the FEM–BEM model with external and internal air volumes modeled. In the next section, these simulation results are compared with the experiments.

3.4. Test–Simulation Comparison

Simulation results are compared with experiments at three points (see Figure 6): point (a) at the center of the envelope (Figure 10), point (b) on the lower part of the envelope (Figure 11) and point (c) at the center of the bottom (Figure 12). The measurements on the envelope (vertical configuration shown in Figure 3) were performed with a 100 dB SPL excitation level, while the measurements on the bottom (horizontal configuration shown in Figure 5) were performed with a 110 dB SPL excitation level. The corresponding excitation levels were used to obtain the simulation results. The qualitative comparison of the simulation results with the experiments is excellent at the three locations. Both major structural resonances and secondary acoustic resonances are well correlated with the experimental resonances.

The PSD levels are also coherent over the whole frequency range ([100–2200 Hz]). The RMS levels corresponding to experiments and simulations are shown in Table 1. The differences are lower than 6 dB. With such good test–simulation correlation, simulation helps to interpret the experimental resonances. Figure 13 highlights the four first resonances in the simulated response at the center of the bottom. In this frequency band [100 Hz, 600 Hz], the numerical modal analysis of the structure, without any acoustic coupling, presents a unique structural mode of the bottom at 407.8 Hz. This mode enables an explanation of the main resonance in Figure 13 at 411 Hz.

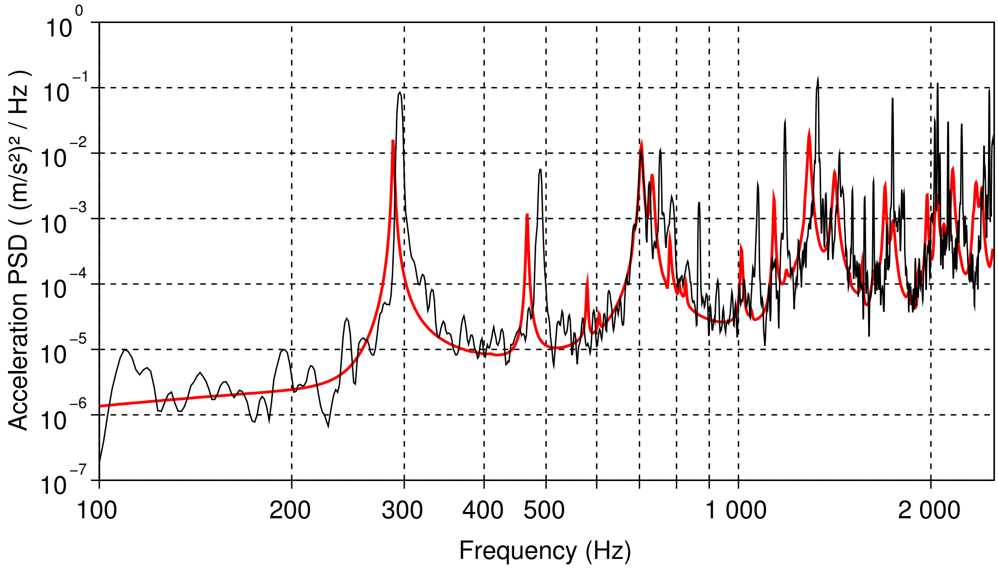

Figure 10. Acceleration PSD at point (a) on the envelope (see Figure 6) with comparison between the experimental data (black) and simulation results (red).

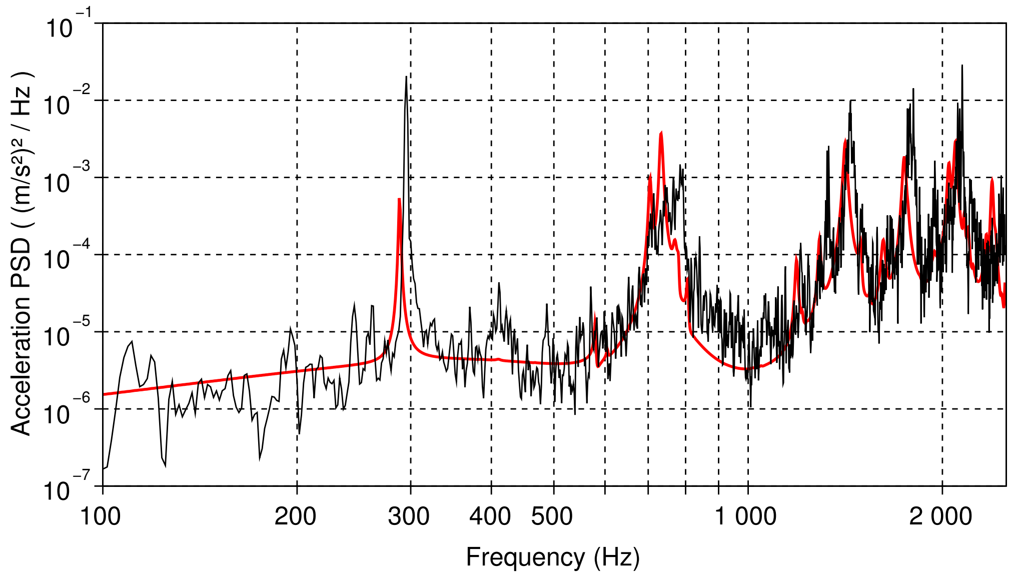

Figure 11. Acceleration PSD at point (b) on the envelope (see Figure 6) with comparison between the experimental data (black) and simulation results (red).

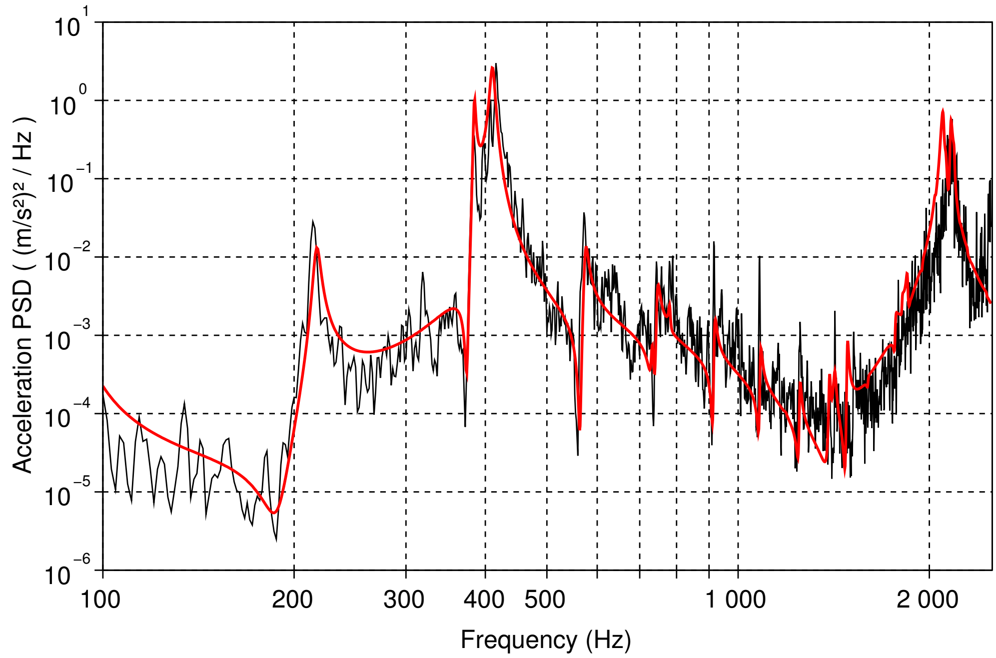

Figure 12. Acceleration PSD at at point (c) on the bottom (see Figure 6) with comparison between the experimental data (black) and simulation results (red).

The frequency shift is due to acoustic coupling. The three other resonances in Figure 13 must be due to acoustic resonances. In order to demonstrate these resonances, a view of the internal acoustic pressure field simulated at those frequencies is presented in Table 2. The three resonances correspond to different acoustic mode shapes. The experimental results thus confirm that acoustic resonances affect the bottom response. This validates the vibroacoustic model with the internal and external air volumes modeled in a BEM subsystem.

Table 1. Test–simulation comparison of the overall RMS level (in the [100–2200 Hz] range) for the three locations studied.

Point	Experiment	FEM–BEM Simulation	Difference
(a)	2.19 m·s^2	1.12 m·s^2	−5.8 dB
(b)	0.96 m·s^2	0.63 m·s^2	−3.6 dB
(c)	6.82 m·s^2	9.06 m·s^2	+2.5 dB

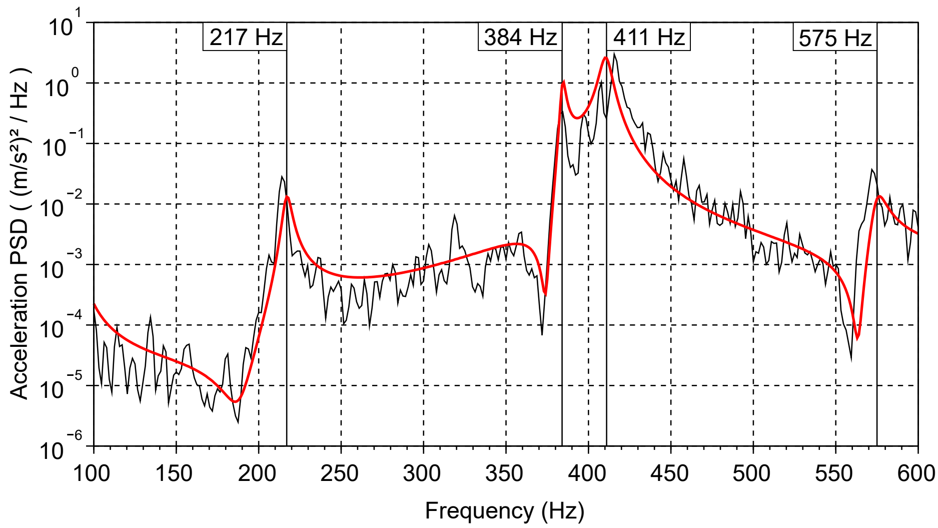

Figure 13. Zoom of Figure 12 below 600 Hz.

Table 2. Interpretation of the four first simulated resonance phenomena (see Figure 13).

Frequency	Mode	Mode Shape
217 Hz	First acoustic resonance	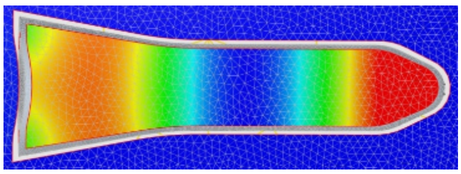
384 Hz	Second acoustic resonance	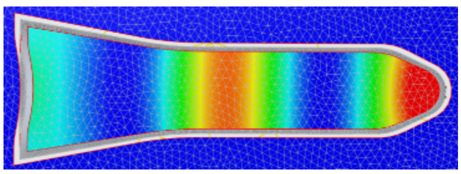
411 Hz	First bottom structural mode	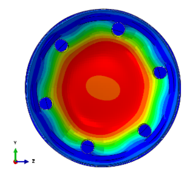
575 Hz	Third acoustic resonance	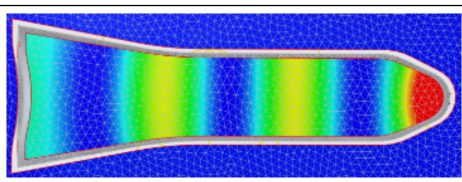

4. SEA Modeling

In the low-frequency range, the FEM–BEM modeling described previously proven to be relevant to predict vibroacoustic responses. At high frequencies, this ability is limited by the modal truncation. As modal density increases at high frequencies, a modal truncation at a significantly higher frequency (≫2500 Hz) would greatly increase the computational cost of the method. At these frequencies, the main expected engineering result is only the overall root mean square acceleration level.

Thus, a complementary method was used to evaluate the vibroacoustic response levels until 16 kHz with a low computational cost: Statistical Energy Analysis (SEA). The theory of the method is quickly introduced in the next section. The setup of the SEA model is then described, including dedicated experiments for the identification of key parameters. Finally, the simulation results are compared with diffuse acoustic field measurements.

4.1. SEA Equations and Hybrid FE–SEA Periodic Theory

In SEA, a complex vibroacoustic structure is represented as an assembly of coupled subsystems that can receive, store, dissipate and transfer energy. By adopting a statistical description of the local dynamic properties of each subsystem, it is possible to predict the overall average response of a complex system across a broad frequency range.

The basic SEA equations express the energy balance in the dynamic response model, which comprises a set of subsystems described by their gross geometric form and dynamic material properties. For a structure made of n subsystems, for every subsystem i, the energy conservation can be written as [17]:

$$P_{i,in} = P_{i,diss} + \sum_{j=1,\neq i}^{n} P_{ij}, \tag{5}$$

$P_{i,in}$ is the input power in subsystem i that is known. The dissipated power in subsystem i ($P_{i,diss}$) and the power transferred from subsystem i to subsystem j (P_{ij}) are modeled as:

$$P_{i,diss} = \omega \eta_{ii} \langle E_i \rangle, \tag{6}$$

$$P_{ij} = \omega(\eta_{ij}\langle E_i \rangle - \eta_{ji}\langle E_j \rangle) \tag{7}$$

where η_{ii} is the damping loss factor (DLF) (or internal loss factor) and η_{ij} is the coupling loss factor (CLF) between subsystem i and subsystem j. The brackets $\langle\rangle$ denote spatial the average of the energies and will be omitted hereafter for simplicity. The coupling loss factors η_{ij} and η_{ji} are related by the expression:

$$N_i \eta_{ij} = N_j \eta_{ji}, \tag{8}$$

where $N_{i,j}$ is the modal density of subsystems i, j. Equation (7) can then be written as:

$$P_{ij} = \omega \eta_{ij} N_i \left(\frac{E_i}{N_i} - \frac{E_j}{N_j} \right). \tag{9}$$

By substituting Equations (6) and (9) in the energy conservation Equation (5), the following set of linear equations is obtained:

$$\omega \begin{bmatrix} N_1 \sum_j \eta_{1j} & -N_1\eta_{12} & \cdots & -N_1\eta_{1n} \\ -N_2\eta_{21} & N_2 \sum_j \eta_{2j} & \cdots & -N_2\eta_{2n} \\ \vdots & \vdots & \ddots & \vdots \\ -N_n\eta_{nl} & -N_n\eta_{n2} & \cdots & N_n \sum_j \eta_{nj} \end{bmatrix} \begin{bmatrix} E_1/N_1 \\ E_2/N_2 \\ \vdots \\ E_n/N_n \end{bmatrix} = \begin{bmatrix} P_{inj,1} \\ P_{inj,2} \\ \vdots \\ P_{inj,n} \end{bmatrix}. \tag{10}$$

Therefore, knowing the injected power and the loss factors, the energies E_i of the subsystems can be determined.

The traditional approach to SEA modeling typically involves the description of a complex system in terms of a number of simpler connected subsystems. These SEA subsystems are usually chosen in a fixed formulation library, in order to fit the real geometry as closely as possible. However, traditional SEA codes often have somewhat limited libraries of subsystems that are based on analytical derivations of wave propagation and scattering in simplified cross-section. Such cross-sections are adequate for simple systems; however, they are often not general enough to rigorously describe the vibroacoustic behavior of complex structures.

The results presented in this article were obtained with Wave6 software, where a statistical energy analysis formulation using finite element and periodic structure theory, called hybrid FE–SEA periodic theory, was implemented [21,30,32]. One of the main advantages of this formulation is the ability to compute some of the parameters involved in the SEA method, such as the coupling loss factors and modal density for complex structures. These parameters are usually calculated analytically only for simple structures [17,33] or need the development of experimental techniques [34,35].

The hybrid FE–SEA method offers a way to use deterministic and statistical subsystems in the same model by coupling them at their boundaries. Each 2D SEA subsystem is described by a unit cell modeled with structural finite elements. Periodic boundary conditions are then applied to the edges and corners of the cell, and phase constant surfaces are obtained by solving an algebraic eigenvalue problem. The SEA parameters can then be related to certain properties of the phase surfaces of the unit cell [32]. The approach enables an arbitrary amount of details to be included in the cross-section of each subsystem, such as curvature or stress stiffening [36].

The first task when setting up a SEA model is to define the subsystem partitioning and the damping loss factors of each subsystem. This is done here using experimental measurements.

4.2. Definition of SEA Subsystems and Estimation of Damping Loss Factors

One of the main difficulties of SEA modeling is the definition of the subsystems in such a way that the conditions of applicability of SEA theory are respected. These conditions are the following [17]:

- an adequate modal density for each subsystem (at least three modes per frequency band),
- a spatial mode covering (the modes used to calculate the modal density must affect all the subsystem), and
- a weak coupling between subsystems.

The experimental measurements presented here make it possible to determine the SEA subsystems of the HB–2 structure in order that the conditions mentioned above should be respected. Furthermore, the damping loss factor of each subsystem, which is a key parameter of the model, is measured.

The test setup is illustrated in Figure 14a. The entire structure was freely suspended and driven sequentially at 11 points, denoted E_i in Figure 14b, using a shaker attached to the excitation point. Analogously to the experimental setup for the vibrometry measurement shown in Figures 3 and 5, the structure is suspended horizontally for an excitation point on the bottom, and vertically for an excitation point on the envelope. For each excitation, the resulting vibration responses were recorded with 21 accelerometers, denoted as A_i in Figure 14b at randomly selected locations so that the spatial average could be estimated. The structure was excited with a white noise from 500 Hz to 16 kHz.

The first clear division of the structure into subsystems is the separation of the bottom and the envelope. Then, the analysis of the FRF measurements at different locations enables the determination of the envelope's subsystems. The envelope is not homogeneous with stiffened zones and zones of different curvature. First, analysis of the measurements is performed by splitting the envelope where its curvature changes. As depicted in Figure 14b, three zones, designated ENV1, ENV2, ENV3, are defined.

All the signals recorded by the accelerometers located in each zone are averaged together. Figure 15 shows the absolute value of the average point mobility Y_{ii} obtained in each zone. The mobility measured in the two zones ENV1 and ENV2 appear to be similar, thereby, revealing strong coupling between these two zones. The ENV3 zone appears to be less coupled to the others. Indeed, the envelope in this zone possesses more stiffeners.

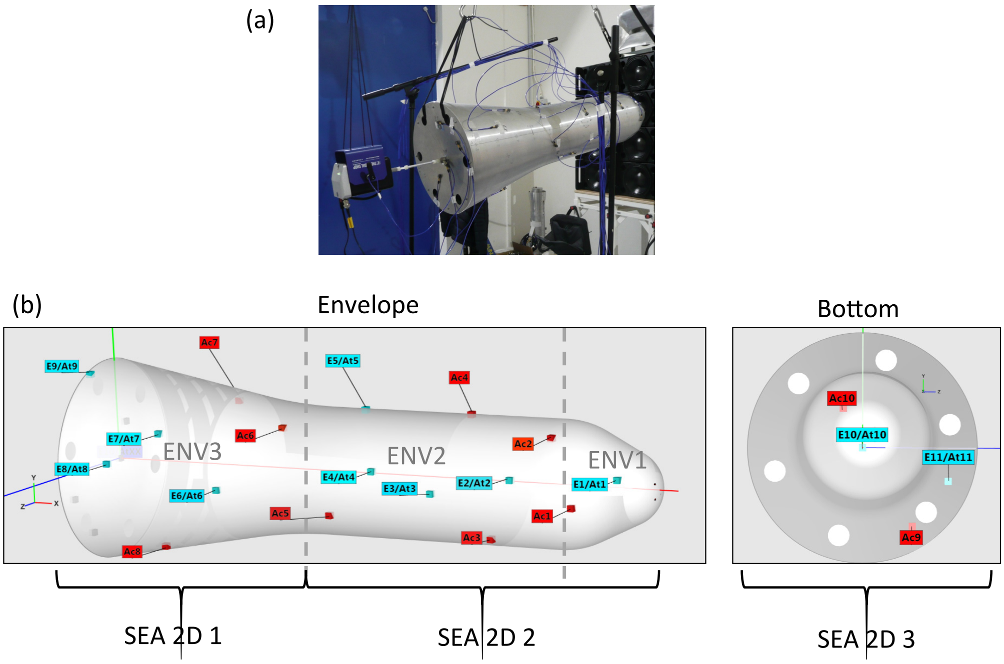

Figure 14. (**a**) The experimental setup. (**b**) HB–2 subsystem definition and the location of the excited and measured points. The blue dots indicate the points that were used for both excitation and response measurement. The red dots indicate the points that were used only for the acceleration response measurement.

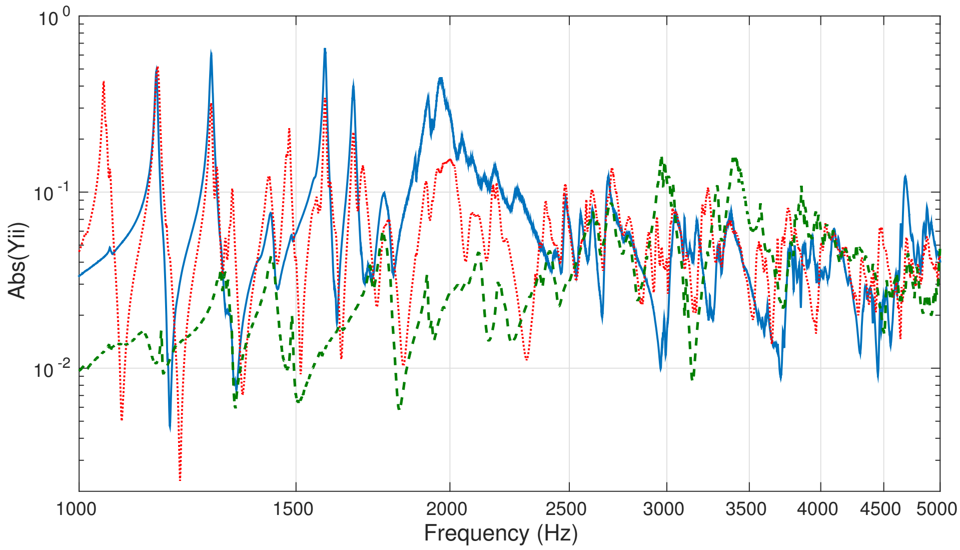

Figure 15. The average mobility measurements for ENV1 (blue line), ENV2 (red dotted line) and ENV3 (green dashed line) zones.

Therefore, the best choice of SEA subsystems for the HB–2 structure is the following: two subsystems for the envelope, designated SEA 2D 1 (for the ENV3 zone) and SEA 2D2 (for the ENV1-ENV2 zones grouped together), and one subsystem for the bottom, designated SEA 2D 3 (see Figure 14b).

The second objective of the experiments is the determination of the damping loss factors. The DLF of each subsystem are calculated with the decay-rate method [17]. They are related to the decay rate (DR) by:

$$\eta_{ii} = \frac{DR}{27.3f}. \tag{11}$$

For each accelerometer, the impulsive time response is measured using a fast process involving correlated time sequences with a low crest factor. One impulsive time response is plotted in Figure 16b. The signals obtained are time filtered for each third octave band. Then, as depicted in Figure 16a, the Energy Time Curve (ETC) is plotted as well as the Schroeder integration [37]. The Decay Rate (DR) is deduced from this integration. The DR corresponds to the time after which the residual integration dropped by −10 dB.

As illustrated in Figure 16a, the chosen starting point is when the integration drops by 0.1 dB. For each frequency band and each measured point, the ETC is plotted, the DR is calculated, and the DLF is deduced using Equation (11). This allows, for each SEA subsystem, a statistical determination of the damping loss factors with a spatial average over various excitation points.

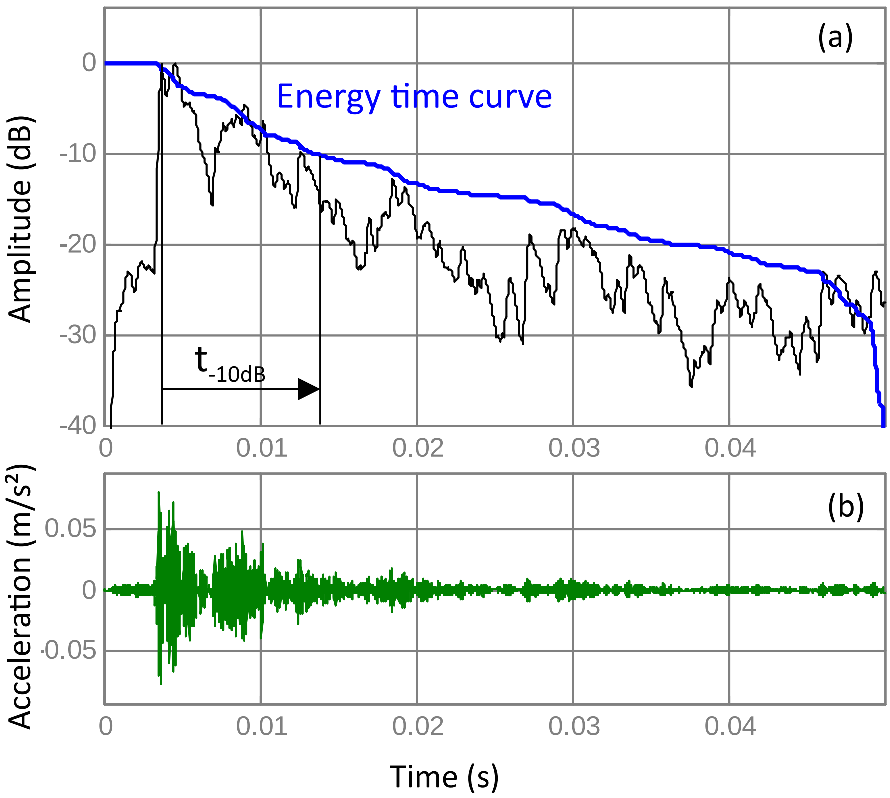

Figure 16. (**a**) Example of Schroeder integration and energy time curve calculations (blue curve) (**b**) Corresponding impulsive time response.

The DLFs obtained for each subsystem are represented in Figure 17 by the mean, minimum and maximum estimated values. The values range from 0.25% to 1% for the envelope and from 1% to 3% for the bottom.

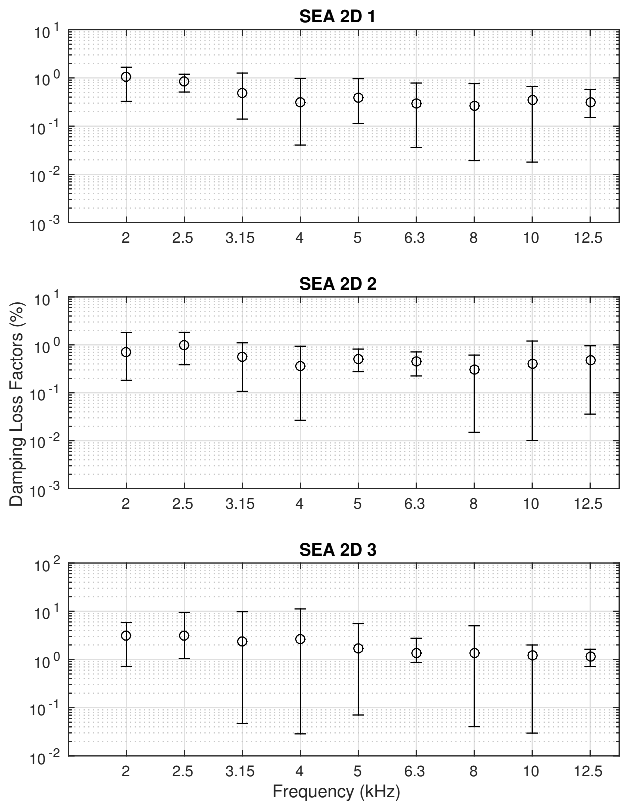

Figure 17. Damping loss factors obtained experimentally for each SEA subsystem.

4.3. SEA Model

Figure 18 illustrates the SEA model in Wave6. Three 2D SEA subsystems are created for the bottom and the two envelope parts. They consist of a double curved shell with an aluminum cross section of 1 mm. The cross-section of the subsystems is described by a unit cell with a single QUAD8 shell element. The mean value of the damping loss factors obtained by experiments (see Figure 17) are defined in each subsystem.

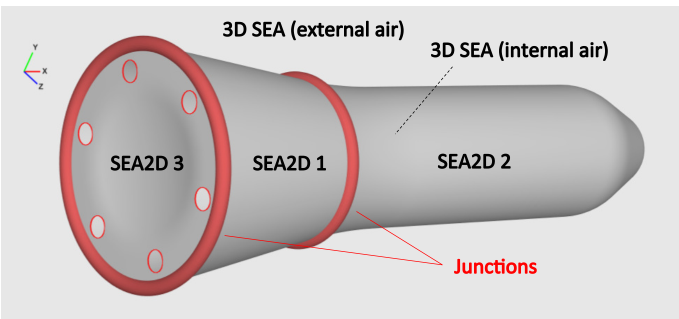

Figure 18. SEA model of the HB2 aeroshell with the surrounding air volumes.

The external air volume and the internal air cavity are modeled with 3D SEA subsystems. The excitation source is a diffuse acoustic field as defined in Section 2.2. Junctions between all the 2D and 3D SEA subsystems and the source are then created.

Line junctions are created between the 2D SEA subsystems, and area junctions are created between the source and the 2D and 3D SEA subsystems, with particular area junctions through the holes of the bottom between the external and internal air volumes. A SEA model is usually valid when there are at least three modes per frequency band. This criterion is estimated from modal analysis at low frequencies and is confirmed with the observed experimental resonances. We achieved above 1250 Hz for the envelope subsystems and above 1600 Hz for the bottom subsystem.

4.4. Test–Simulation Comparison

Figure 19 shows the mean RMS acceleration of each subsystem in the third octave bands. The simulated results (blue lines) are compared with experimental data obtained by laser vibrometry measurements (black lines with stars). The time acceleration response is measured at several points of each subsystem (46 and 20 measurements on a line along the x-axis for the subsystems SEA 2D 1 and SEA 2D 2, and 175 measurements covering all the surface for the bottom subsystem SEA 2D 3).

The Power Spectral Density is then computed for each point. Then, for each subsystem, a spatial average of the PSD of all points belonging to the subsystem is performed. As explained in Section 2.3, with scanning laser vibrometry, the measurements at different points are not synchronous but sequential, allowing only the computation of the PSD S_i and not the cross power spectral densities S_{ij} between two points i, j.

Thus, the experimental results shown in Figure 19 correspond to the average of the PSD (equal to $(S_i + S_j)/2$), which would be overestimated compared to the real average value, which accounts for cross spectral densities $((S_i + S_j)/4) + S_{ij}/2)$. Finally, the averaged PSD value of each subsystem is converted to RMS acceleration in each third octave band. The results shown in Figure 19 show good test–simulation correlation. In subsystem SEA 2D 1, an averaged difference of -1.9 dB between the mean simulation results and measurements is observed.

In subsystem SEA 2D 2, this difference reaches -3.8 dB, revealing a slight underestimation of levels by SEA simulation or a slight overestimation of the experimental averaged PSD because of the lack of cross-spectral PSD data. In subsystem SEA 2D 3, simulation underestimates levels below 2.8 kHz; however, above 2.8 kHz, the averaged difference between simulation and experiments is only -1.1 dB.

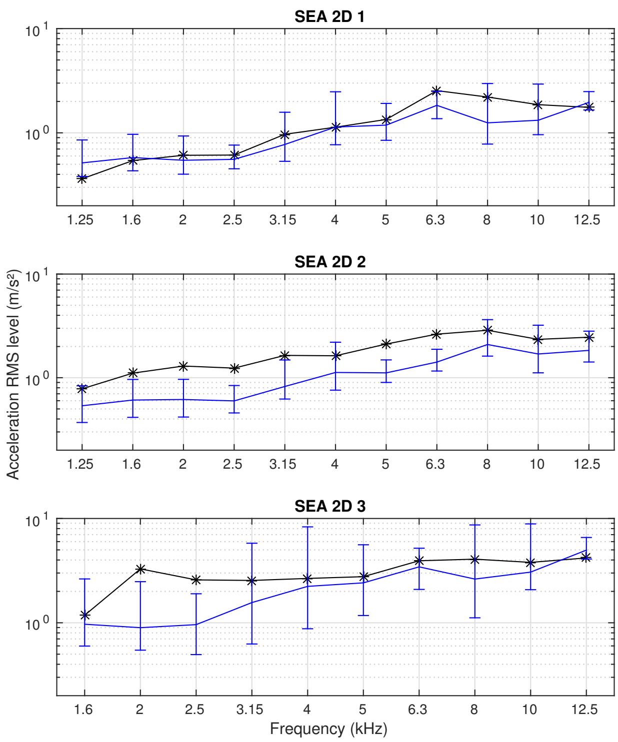

Figure 19. Test (black lines with stars) -simulation (blue lines) comparison for one-third octave band mean acceleration in the three SEA subsystems. The simulation spread displayed is obtained varying the damping loss factor in accordance with measurements shown in Figure 17.

5. Full-Frequency Test–Simulation Comparison

The FEM–BEM and SEA results are combined together to obtain full-frequency simulation results. The boundary between the two methods has to be set strictly beyond the validity criterion of the SEA model (>1600 Hz) and strictly below the limit of the modal truncation of the FEM model (2500 Hz). This boundary was set at 2200 Hz in order to include the second bottom resonance (around 2100 Hz) in the low-frequency range. FEM–BEM simulation provides the response acceleration PSD for every mesh point, with a fine frequency resolution, whereas SEA simulation provides a mean acceleration level per frequency band.

From an industrial perspective, the first expected output of a full-frequency simulation tool is the overall root mean square acceleration level at every point of the structure. For this purpose, for every point studied, the RMS level computed below 2200 Hz using FEM–BEM can be summed with the mean RMS level beyond 2200 Hz of the SEA subsystem to which the point belongs (using a quadratic sum). The second level of analysis is the frequency content of the simulated response.

For this analysis, the one-twelfth-octave band representation is chosen. The acceleration PSD measured is integrated in every one-twelfth-octave band to obtain the proper representation, and the FEM–BEM results are processed in the same way. The SEA simulation shown in Section 4 is carried out again choosing the one-twelfth-octave band discretization. When working in one-twelfth-octave band, the SEA criteria (at least three modes per frequency band) is validated above 1600 Hz for the envelope subsystems and above 2000 Hz for the bottom.

Yet, in this last simulation, the DLF that were defined based on one-third-octave band measurement remain the same so that they are constant along each one-third-octave band. The results obtained are shown at three points located in the three SEA subsystems:

- point (a) at the center of the envelope, located in SEA 2D 2, see Figure 20,
- point (b) located on the envelope, in SEA 2D 1 subsystem, see Figure 21, and
- point (c) on the bottom, located in SEA 2D 3, see Figure 22.

A very good test–simulation agreement is observed in the full-frequency range, which proves the complementarity between the FEM–BEM and SEA methods. The corresponding RMS levels are presented in Table 3.

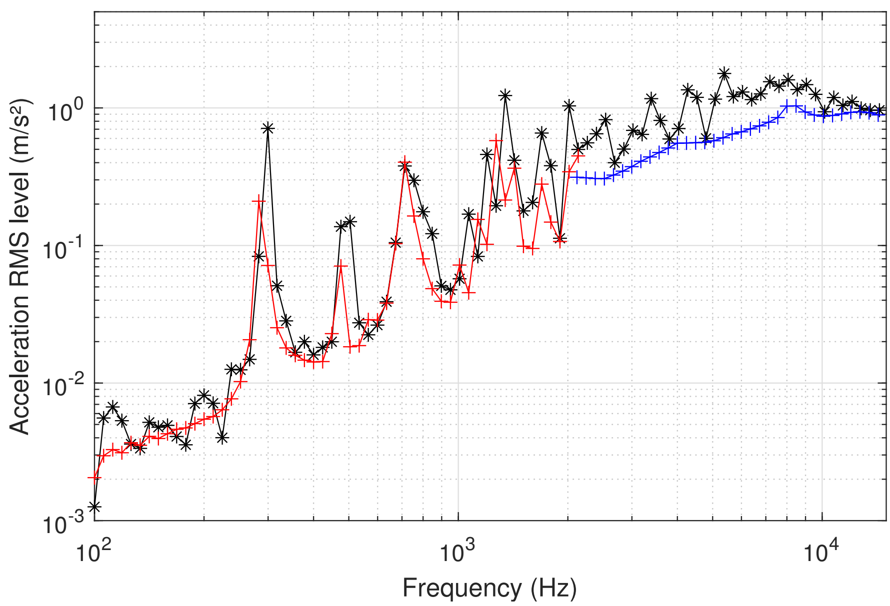

Figure 20. Full-frequency test–simulation comparison at point (a), one-twelfth-octave frequency band representation. The experimental response (black curve with stars) is compared with the combination of the FE-BEM results (red curve with +) and SEA results (blue curve with +).

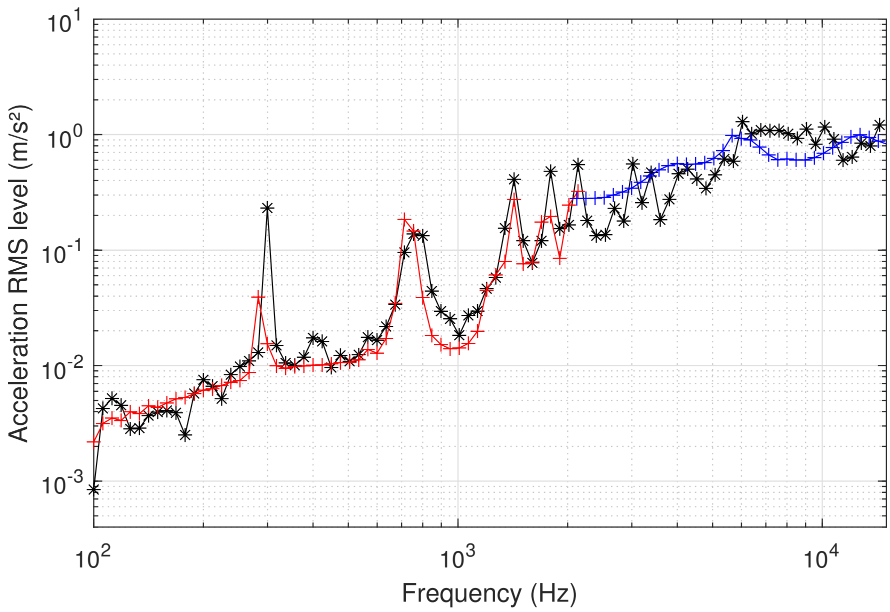

Figure 21. Full-frequency test–simulation comparison at point (b), one-twelfth-octave frequency band representation. The experimental response (black curve with stars) is compared with the combination of the FE-BEM results (red curve with +) and SEA results (blue curve with +).

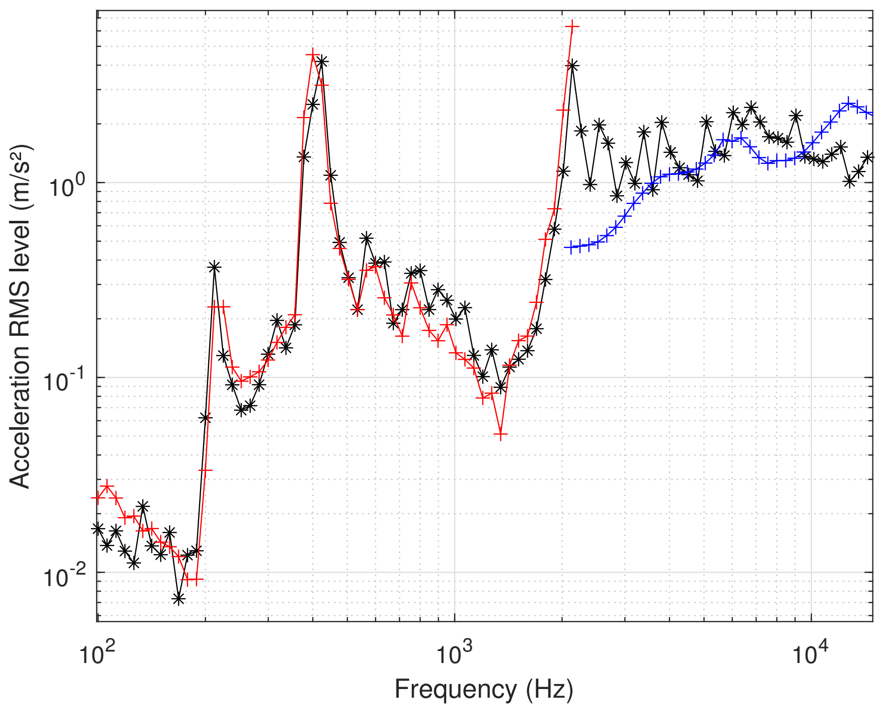

Figure 22. Full-frequency test–simulation comparison at point (c) on the bottom, one-twelfth-octave frequency band representation. The experimental response (black curve with stars) is compared with the combination of the FE-BEM results (red curve with +) and SEA results (blue curve with +).

Table 3. Test–simulation comparison of the overall RMS level, in the [100 Hz, 15 kHz] range, for the three locations studied.

Point	FEM–BEM [100–2200] Hz	SEA Simulation [2.2–15] kHz	Full-Frequency Simulation	Experiment [0.1–15] kHz	Difference
(a)	1.12 $m \cdot s^{-2}$	4.04 $m \cdot s^{-2}$	4.19 $m \cdot s^{-2}$	6.71 $m \cdot s^{-2}$	−4.1 dB
(b)	0.63 $m \cdot s^{-2}$	3.91 $m \cdot s^{-2}$	3.96 $m \cdot s^{-2}$	4.40 $m \cdot s^{-2}$	−0.9 dB
(c)	9.06 $m \cdot s^{-2}$	8.56 $m \cdot s^{-2}$	12.46 $m \cdot s^{-2}$	11.38 $m \cdot s^{-2}$	0.8 dB

6. Conclusions

This work is a step towards the simulation of the vibroacoustic response of a ballistic vehicle during flight. Beyond the difficulties of characterizing in-flight pressure fluctuations, which are not addressed in this study, a detailed vibroacoustic model of the vehicle is needed. A test structure representing an aeroshell was modeled using finite elements and Statistical Energy Analysis. This model was validated through diffuse acoustic field testing.

A dedicated experimental setup in a reverberant chamber was developed. In the low-frequency range, the test–simulation comparison highlights the need to model the air volume surrounding the structure to consider internal acoustic resonances and scattering effects. With BEM modeling of the surrounding air volumes, the simulation results are close to the experimental data, with a maximum 6 dB difference.

In the high-frequency range, two key steps were necessary to set up the SEA model: experimental identification of the Damping Loss Factor using a dedicated ground experiment and the use of a periodic FE–SEA method for the modeling of each subsystem and the computation of the Coupling Loss Factors. The results obtained with this model are in accordance with the mean responses in each subsystem.

A slight underestimation of the response level in the upper side of the envelope was observed (−3.8 dB); yet, this simulation–test agreement is sufficient to validate the model. The FEM–BEM and SEA results are complementary to obtain the full-frequency vibroacoustic response. For each simulation point studied, the estimated high-frequency response is the average value in the subsystem to which the point belongs, calculated using the SEA.

Good test–simulation agreement was observed with a maximum difference of −4.1 dB. For the particular structure under study, the boundary between the FE-BEM and SEA frequency domains was set at 2200 Hz. The full-frequency test–simulation comparison shows that this boundary is well-suited for the envelope and is slightly low considering the bottom of the structure.

The model could thus be improved by including more modes in the FEM–BEM analysis and by shifting the boundary with the SEA domain towards high frequencies. Another improvement could be the introduction of an additional mid-frequency model, such as an FE–SEA model. Regarding the industrial application, the full-frequency model described meets the need to forecast dynamic responses.

Author Contributions: Formal analysis, M.C. and H.V.C.; Investigation, M.C., H.V.C. and B.A.; Methodology, M.C., H.V.C. and B.A.; Writing—original draft, M.C. and H.V.C.; Writing—review & editing, B.A. All authors have read and agreed to the published version of the manuscript.

Funding: This research received no external funding.

Data Availability Statement: Not applicable.

Acknowledgments: The authors acknowledge the CEA/CESTA teams involved in this project: the team that developed the acoustic experimental setup, the team that designed and engineered the test structure and the team that ran the experiments. The authors also acknowledge the Polytec team that performed the laser vibrometer measurements and the Dassault System—Wave6 team that helped with the modeling.

Conflicts of Interest: The authors declare no conflict of interest.

References

1. Corcos, G.M. Resolution of pressure in turbulence. *J. Acoust. Soc. Am.* **1963**, *35*, 192–199. [CrossRef]
2. Bull, M.K. Wall-pressure fluctuations associated with subsonic turbulent boundary layer flow. *J. Fluid Mech.* **1967**, *28*, 719–754. [CrossRef]
3. Goody, M. Empirical spectral model of surface pressure fluctuations. *AIAA J.* **2004**, *42*, 1788–1794. [CrossRef]
4. Houbolt, J.C. *Structural Response of Re-Entry Vehicles to Boundary Layer Noise*; Technical Report 35; Aeronautical Research Associates of Princeton Inc.: Princeton, NJ, USA, 1965.
5. Lowson, M.V. *Prediction of Boundary Layer Pressure*; Technical Report; Wyle Laboratories: Huntsville, AL, USA, 1968.
6. Laganelli, A.L.; Howe, J.R. *Prediction of Pressure Fluctuations Associated with Maneuvering Re-Entry Weapons*; Technical Report 59; Air Force Flight Dynamics Laboratory: Dayton, OH, USA, 1977.
7. Beresh, S.J.; Henfling, J.F.; Spillers, R.W.; Pruett, B.O. Fluctuating wall pressures measured beneath a supersonic turbulent boundary layer. *Phys. Fluids* **2011**, *23*, 075110. [CrossRef]
8. Smith, J.A.; Dechant, L.J.; Mesh, M.; Casper, K.M. Comparison of a Turbulent Boundary Layer Pressure Fluctuation Model to Hypersonic Cone Measurements. In Proceedings of the 34th AIAA Applied Aerodynamics Conference, Washington, DC, USA, 13–17 June 2016.
9. Juliano, T.J.; Adamczak, D.; Kimmel, R.L. HIFiRE-5 flight test results. *J. Spacecr. Rocket.* **2015**, *52*, 650–663. [CrossRef]
10. Hong, C.; Shin, K.K. Modeling of wall pressure fluctuations for finite element structural analysis. *J. Sound Vib.* **2010**, *329*, 1673–1685. [CrossRef]
11. Bonness, W.K.; Fahnline, J.B.; Lysak, P.D.; Shepherd, M.R. Modal forcing functions for structural vibration from turbulent boundary layer flow. *J. Sound Vib.* **2017**, *395*, 224–239. [CrossRef]
12. Citarella, R.; Federico, L.; Cicatiello, A. Modal acoustic transfer vector approach in a FEM–BEM vibro-acoustic analysis. *Eng. Anal. Bound. Elem.* **2007**, *31*, 248–258. [CrossRef]
13. Citarella, R.; Landi, M. Acoustic analysis of an exhaust manifold by Indirect Boundary Element Method. *Open Mech. Eng. J.* **2011**, *5*, 138–151. [CrossRef]
14. Atalla, N.; Sgard, F. *Finite Element and Boundary Methods in Structural Acoustics and Vibration*; CRC Press: Boca Raton, FL, USA, 2015.
15. Montgomery, J. Modeling of Aircraft Structural-Acoustic Response to Complex Sources Using Coupled FEM/BEM Analyses. In Proceedings of the tenth AIAA/CEAS Aeroacoustics Conference, Manchester, UK, 10–12 May 2004; p. 2822.
16. Li, Y.; Fei, Q.; Wu, S.; Zhang, P.; Jiang, D. Vibro-acoustic coupled analysis excited by correlated turbulent boundary layer. *J. Vibroengineering* **2016**, *18*, 3225–3241.
17. Lyon, R. *Statistical Energy Analysis of Dynamical Systems: Theory and Applications*; MIT Press: Cambridge, MA, USA, 1975.
18. Petrone, G.; Melillo, G.; Laudiero, A.; De Rosa, S. A Statistical Energy Analysis (SEA) model of a fuselage section for the prediction of the internal Sound Pressure Level (SPL) at cruise flight conditions. *Aerosp. Sci. Technol.* **2019**, *88*, 340–349. [CrossRef]
19. Desmet, W.; Pluymers, B.; Atak, O. *MID-FREQUENCY-CAE Methodologies for Mid-Frequency Analysis in Vibrations and Acoustics*; Faculty of Engineering, Katholieke Universiteit Leuven: Leuven, Belgium, 2012.
20. Ladevèze, P.; Arnaud, L.; Rouch, P.; Blanzé, C. The variational theory of complex rays for the calculation of medium-frequency vibrations. *Eng. Comput.* **2001**, *18*, 193–214. [CrossRef]
21. Cotoni, V.; Shorter, P.; Langley, R. Numerical and experimental validation of a hybrid finite element-statistical energy analysis method. *J. Acoust. Soc. Am.* **2007**, *122*, 259–270. [CrossRef] [PubMed]
22. Peiffer, A. Full frequency vibro-acoustic simulation in the aeronautics industry. In Proceedings of the ISMA 2016, Leuven, Belgium, 19–21 September 2016; pp. 1–15.
23. Daley, M.J.; Hambric, S.A. Simulating and Measuring Structural Intensity Fields in Plates Induced by Spatially and Temporally Random Excitation. *J. Vib. Acoust.* **2005**, *127*, 451–457. [CrossRef]
24. Marchetto, C.; Maxit, L.; Robin, O.; Berry, A. Vibroacoustic response of panels under diffuse acoustic field excitation from sensitivity functions and reciprocity principles. *J. Acoust. Soc. Am.* **2017**, *141*, 4508–4521. [CrossRef] [PubMed]
25. Hamdi, M.A.; Omrani, A.; Zerbib, N.; Gardner, B. Simulation of random response of typical CFRP space structure panels submitted to a diffuse sound field comparison between test and analysis results. In Proceedings of the 11th European Conference on Spacecraft Structures, Materials and Mechanical Testing, Toulouse, France, 14–16 September 2009.
26. Li, P.; Yan, Y.; Lin, H. Numerical simulation and experimental researches on the vibration-acoustic coupled property of an aircraft model under strong reverberation noise. *J. Vib. Control* **2017**, *23*, 2757–2766. [CrossRef]
27. Zhang, G.; Yan, Y. Vibro-acoustic response analysis and experimental verification of aircraft based on statistical energy analysis. In Proceedings of the first International Conference on Mechanical Engineering and Material Science, Shanghai, China, 28–30 December 2012.
28. Yan, Y.; Li, P.; Lin, H. Analysis and experimental validation of the middle-frequency vibro-acoustic coupling property for aircraft structural model based on the wave coupling hybrid FE-SEA method. *J. Sound Vib.* **2016**, *371*, 227–236. [CrossRef]
29. Gray, J.D. *Summary Report on Aerodynamic Characteristics of Standard Models HB-1 and HB-2*; Technical Report; Arnold Engineering Development Complex: Tullahoma, TN, USA, 1964.

30. Shorter, P.J.; Langley, R.S. On the reciprocity relationship between direct field radiation and diffuse reverberant loading. *J. Acoust. Soc. Am.* **2005**, *117*, 85–95. [CrossRef]
31. Langley, R.S. Numerical evaluation of the acoustic radiation from planar structures with general baffle conditions using wavelets. *J. Acoust. Soc. Am.* **2007**, *121*, 766–777. [CrossRef]
32. Cotoni, V.; Langley, R.; Shorter, P. A statistical energy analysis subsystem formulation using finite element and periodic structure theory. *J. Sound Vib.* **2008**, *318*, 1077–1108. [CrossRef]
33. Lyon, R.H.; Eichler, E. Random vibration of connected structures. *J. Acoust. Soc. Am.* **1964**, *36*, 1344–1354. [CrossRef]
34. Bies, D.; Hamid, S. In situ determination of loss and coupling loss factors by the power injection method. *J. Sound Vib.* **1980**, *70*, 187–204. [CrossRef]
35. Bouhaj, M.; Von Estorff, O.; Peiffer, A. An approach for the assessment of the statistical aspects of the SEA coupling loss factors and the vibrational energy transmission in complex aircraft structures: Experimental investigation and methods benchmark. *J. Sound Vib.* **2017**, *403*, 152–172. [CrossRef]
36. Shorter, P.; Legault, J.; Caro, S.; Langley, R. A new generalized approach to Statistical Energy Analysis (SEA). In Proceedings of the INTER-NOISE and NOISE-CON Congress and Conference Proceedings, Hamburg, Germany, 21–24 August 2016; Institute of Noise Control Engineering: West Lafayette, IN, USA, 2016; Volume 253, pp. 7392–7403.
37. Davis, D.; Martinson, J. Using Basic Energy Time Curve (ETC) Measurements. In Proceedings of the Audio Engineering Society Convention 66, Los Angeles, CA, USA, 6–9 May 1980; Audio Engineering Society: New York, NY, USA, 1980.